

## A SURVEY OF SIO 5→4 EMISSION TOWARDS OUTFLOWS FROM LOW-LUMINOSITY PROTOSTELLAR CANDIDATES

ANDY G. GIBB

Department of Astronomy, University of Maryland, College Park, MD 20742, USA  
agg@astro.umd.edu

JOHN S. RICHER

Cavendish Astrophysics Group, Department of Physics, University of Cambridge, Madingley Road,  
Cambridge, CB3 0HE, UK  
jsr@mrao.cam.ac.uk

CLAIRES J. CHANDLER

National Radio Astronomy Observatory<sup>a</sup>, PO Box O, Socorro, NM 87801, USA<sup>a</sup> The National Radio Astronomy Observatory is a facility of the National Science Foundation operated under cooperative agreement by Associated Universities, Inc.  
cchandle@nrao.edu

AND

CHRIS J. DAVIS

Joint Astronomy Centre, 660 N. A'ohōkū Place, Hilo, HI 96725, USA  
c.davis@jach.hawaii.edu*Draft version December 7, 2018*

## ABSTRACT

We have observed the SiO  $J=5\rightarrow4$  line towards a sample of 25 low-luminosity ( $L_* < 10^3 L_\odot$ ) protostellar outflow systems. The line was detected towards 7 of the 25 sources, a detection rate of 28 per cent. The majority (5 out of 7) of sources detected were of class 0 status. We detected a higher fraction of class 0 sources compared with the class I and II sources, although given the small numbers involved the significance of this result should be regarded as tentative. Most of the detected sources showed emission either at or close to the central position, coincident with the protostar. In four cases (HH 211, HH 25MMS, V-380 Ori NE and HH 212) emission was also detected at positions away from the center, and was stronger than that observed at the centre position.

SiO abundances of  $10^{-8}$  to  $8\times10^{-7}$  are derived from LTE analysis. For 2 sources we have additional transitions which we use to conduct statistical equilibrium modeling to estimate the gas density in the SiO-emitting regions. For HH 25MMS these results suggest that the SiO emission arises in a higher-density region than the methanol previously observed. We find that the most likely explanation for the preferential detection of SiO emission towards class 0 sources is the greater density of those environments, reinforced by higher shock velocities. We conclude that while not all class 0 sources exhibit SiO emission, SiO emission is a good signpost for the presence of class 0 sources.

*Subject headings:* stars: formation — ISM: jets and outflows — ISM: molecules — ISM: Herbig-Haro objects — radio lines: ISM

## 1. INTRODUCTION

In principle SiO has great potential as an efficient shock tracer, a millimetre-wavelength counterpart to the near-infrared lines of H<sub>2</sub>. Its abundance in quiescent gas within cloud cores is  $< 10^{-12}$  relative to molecular hydrogen (Irvine, Goldsmith & Hjalmarson 1987; Ziurys, Friberg & Irvine 1989), which can rise to as high as  $10^{-6}$  in outflows (Martín-Pintado et al. 1992). The formation of SiO in post-shock gas probably takes place as a consequence of grain sputtering or grain-grain collisions releasing Si-bearing material into the gas phase which reacts rapidly with O-bearing species (principally O<sub>2</sub> and OH) to form SiO (Schilke et al. 1997; Caselli, Hartquist & Havnes 1997).

A number of outflow sources have been detected in SiO emission (e.g. Martín-Pintado, Bachiller & Fuente 1992) but it is only recently that extensive surveys of outflows

have been carried out and published. Harju et al. (1998) observed the locations of water and/or OH masers, with the result that their sample is dominated by massive young stellar objects (YSOs). Furthermore they only observed at the maser position in each source although they were able to obtain high sensitivity spectra. The sample of Codella, Bachiller & Reipurth (1999) includes YSOs with luminosities in the range 1 to  $10^4 L_\odot$ , and they made the surprise discovery that a number of sources show evidence for high- and low-velocity SiO components with different spatial distributions and linewidths. Furthermore, the abundance of SiO was different in each component, with the high-velocity SiO two orders of magnitude more abundant than the low-velocity SiO. In addition, the low-velocity component was typically only seen in the lower-lying transitions of SiO, probably indicating that the low-velocity gas is also of lower density and/or temperature.

In an effort to understand the conditions under which SiO emission is observed, we have conducted a survey of the  $J=5\rightarrow4$  transition of SiO towards a sample of 25 low-luminosity YSOs, made at the James Clerk Maxwell Telescope (JCMT) on Mauna Kea, Hawaii. The following section describes the observations, with subsequent sections presenting the results, analysis and discussion of the data.

## 2. SAMPLE SELECTION AND OBSERVATIONS

The sources were selected from the list of Fukui et al. (1993) and/or on the basis that comparable H<sub>2</sub> and CO observations existed. While the sample mostly includes low-luminosity class 0 protostars, a number of class I and class II sources (as well as objects of somewhat greater luminosity) are also included to test if the age and luminosity of the driving source is relevant in the production of observable quantities of SiO. Source details are listed in Table 1.

The observations were made over several nights in 1995 October and 1997 September, November and December using the facility receiver A2 which was tuned to observe the  $5\rightarrow4$  SiO transition at 217.1050 GHz. The backend was the digital autocorrelation spectrometer (DAS), using a bandwidth of 500 MHz and an initial spectral resolution of 378 kHz, although the spectra were binned for the reduction and analysis to provide a velocity resolution of 4.2 km s<sup>-1</sup> at 217 GHz. Pointing sources were Uranus, Saturn, 3C 111, W3(OH), NGC 7538-IRS1, NGC 2071-IR, and OMC-1. Pointing was good to 2 or 3 arcsec. NGC 7538-IRS1, NGC 2071-IR and OMC-1 were also used for calibration checks by comparing with standard spectra. Position-switching was employed throughout against a blank region of sky 300–1200 arcsec away.

At 217 GHz, the JCMT beam has a full-width at half-maximum (FWHM) of 22 arcsec. Table 1 lists the important details for the sources observed. Line intensities are reported as  $T_A^*$ , which have been converted to main-beam brightness temperatures,  $T_{\text{MB}}=T_A^*/\eta_{\text{MB}}$  (where the main beam efficiency,  $\eta_{\text{MB}}$ , is 0.71 at 217 GHz), for the purposes of the computations in Section 4.

Additional observations were made of several sources which were either not observed in the previous runs or suffered from poor noise levels, this time with the A3i receiver on 2000 September 4. The backend and switching setups were identical to the previous runs. Pointing and calibration were checked on W3(OH), OMC-1 and NGC 7538-IRS1, and were good to within 2 arcsec and 10 per cent respectively. The main beam efficiency for these observations is 0.7.

Each source was observed at the central position, and in all cases except two, either a grid of points was observed or a strip-map made along the flow axis to cover the extent of the known CO flow or H<sub>2</sub> jet. In most cases this amounted to observing 60 to 200 arcsec away from the source position depending on the size of the flow. If SiO emission was detected along the flow axis then in some cases we observed off-axis positions to determine the extent of the SiO emission (time permitting).

Only L1448-mm and NGC 2071 were observed at a single position. Since SiO has been mapped in both of these sources previously we did not extend our mapping further. RNO 43-mm was observed at a number of positions cover-

ing the extensive CO flow (Bence, Richer & Padman 1996). The innermost portion of the flow between the positions n1 and s1 (Bence et al. 1996) was mapped as far as 150 arcsec from the source, with further mapping carried out at the CO peaks n2, n4, n5 and n6 (Bence et al.), some 200–400 arcsec further north-east. Two more sources were covered in our mapping of other sources: SSV 59 was observed while making the map of HH 25MMS and NGC 2024-FIR6 was observed while mapping the NGC 2024-FIR5 outflow. The details for all the other sources are given in Table 2.

## 3. RESULTS

### 3.1. HH 211-mm

HH 211 is an excellent example of a Class 0 source with a molecular hydrogen jet, driving a highly-collimated CO outflow (Gueth & Guilloteau 1999) perpendicular to a circumstellar disk. Knots of shocked molecular hydrogen emission are observed in a jet-like configuration (McCaughrean, Rayner & Zinnecker 1994). HH 211 exhibits the brightest  $5\rightarrow4$  emission in our sample, with a peak antenna temperature of 0.83 K in the red lobe of the outflow. The bright line and the dual-peaked nature of the line profile led to a successful follow up study with the VLA (Chandler & Richer 2001). The  $1\rightarrow0$  emission extends for approximately 20 arcsec either side of the driving source and shows a velocity gradient along the jet axis with the highest velocity emission farthest from the source. In the transverse direction, the SiO emission extends for only an arcsec either side of the flow axis. Chandler & Richer also show that the  $5\rightarrow4$  emission traces the same kinematic components as the  $1\rightarrow0$ .

Nisini et al. (2002) show an image of the red- and blueshifted lobes of the outflow as seen in SiO  $5\rightarrow4$ . Each lobe peaks symmetrically either side of the driving source and is unresolved in the 22-arcsec beam of the JCMT. The appearance is very similar to single-dish observations of the CO outflow (McCaughrean et al. 1994). Example spectra towards each lobe and the driving source are shown in Figure 1. The two velocity components of the outflow are clearly spectrally resolved. There is virtually no SiO emission at the systemic velocity: the bulk of the emission peaks 10–20 km s<sup>-1</sup> from the rest velocity. The velocity extent of each lobe is approximately 20 km s<sup>-1</sup>. Gaussian fits to spectra at the peak of each lobe give linewidths of  $\sim$ 10–16 km s<sup>-1</sup> (blue lobe) and 15 km s<sup>-1</sup> (red lobe).

### 3.2. HH 25MMS

In our survey, HH 25MMS exhibits the most spatially-extended SiO emission of all the targets in Table 1. HH 25MMS is a deeply-embedded low-luminosity ( $6 L_\odot$ ) class 0 protostar in the L 1630 molecular cloud (Gibb & Davis 1998, hereafter GD98). A compact but highly-collimated CO flow which probably lies close to the plane of the sky is centered on the position of a weak radio continuum source (GD98; Bontemps, André & Ward-Thompson 1995). In addition a number of other molecules are seen in the outflow, in particular CS, CH<sub>3</sub>OH and H<sub>2</sub>CO (GD98).

The SiO emission is undoubtedly associated with the CO outflow (see Fig. 2) although there are significant differences in their respective distribution. The respective CO and SiO peaks are separated by  $\sim$ 35 arcsec with the

SiO peaking at the tip of the CO flow, offset by (36,−57) arcsec from HH 25MMS. The CO peak at (14,−29) is not distinguished in the SiO map. The H<sub>2</sub> knots HH25C and HH25D (Davis et al. 1997a) appear to be closely associated with the SiO, evidence which supports the formation of SiO upstream from bow shocks. However, it is not possible to directly associate the H<sub>2</sub> emission features with any particular SiO feature. Higher resolution observations will undoubtedly help to clarify this relation.

The SiO 5→4 observations of HH 25MMS were tuned to obtain the 6<sub>5</sub>→5<sub>4</sub> line of SO (in the upper sideband at 219.9494 GHz) within the same passband and is clearly detected in HH 25MMS. Figure 2b shows the distribution of SO, which is largely similar to the SiO. The peak SO emission is brighter than the SiO ( $T_A^* \sim 0.9$  K towards the peak position compared with 0.5 K for the SiO), but generally narrower (linewidths typically 4 km s<sup>−1</sup> compared with 9–12 km s<sup>−1</sup> for the SiO). The SO emission has a similar distribution to the methanol seen by GD98, suggesting that the action of the outflow is directly responsible for driving a series of chemical reactions not otherwise possible in the ambient gas.

Since the signal-to-noise ratio is relatively low, little kinematic information can be obtained from velocity channel maps. However, it is still possible to distinguish two velocity components to the SiO emission, one redshifted relative to the line center, the other blueshifted. The dominant component is the redshifted which follows the CO lobe very closely (Fig. 2c), and peaks at the very tip of the flow. The blueshifted component is weaker and peaks approximately 10 arcsec west of HH 25D, giving the SiO image in Fig. 2 its westward skew. The mean SiO linewidth derived from gaussian fits is ∼7.5 km s<sup>−1</sup>, although many of the spectra are not symmetric.

In addition to the 5→4 data, we have a small map of the 7→6 line (GD98) and a single long integration 8→7 spectrum. Unfortunately, the 7→6 map does not extend as far as the tip of the outflow. The 7→6 spectrum shown in GD98 is from the CO peak. The width of the 7→6 line is 8.5 km s<sup>−1</sup>, and it peaks at a velocity redshifted by ∼5 km s<sup>−1</sup> relative to the systemic velocity. The single 8→7 spectrum is also from the CO peak, shown in Fig. 3c. Like the 7→6 line, the 8→7 line at the CO peak is redshifted, centered at +5 km s<sup>−1</sup> relative to the systemic velocity, with a FWHM of 9.9 km s<sup>−1</sup>.

### 3.3. HH 212

HH 212 is also a low-luminosity class 0 protostar associated with the IRAS source 05413–0104 which drives a bipolar H<sub>2</sub> jet (Zinnecker, McCaughrean & Rayner 1998). HH 212 is a water maser source and high-resolution observations have revealed the proper motions of the maser spots in the southern outflow lobe (Claussen et al. 1998). The H<sub>2</sub> jet also drives a well-collimated CO flow (Lee et al. 2000). As seen in Fig. 4, the spectra at the center position and (−8,−18) offset show clear detections. The line at the center position can be fitted by a gaussian of peak  $T_A^* = 0.17$  K with a FWHM of 15.8 km s<sup>−1</sup>, centered at −12.8 km s<sup>−1</sup> relative to the rest velocity of the cloud. The line at the (−8,−18) position is not significantly shifted with respect to the ambient cloud, and is narrower (8.3 km s<sup>−1</sup>).

### 3.4. L 1448-mm

L 1448-mm (also known as L 1448C) drives a remarkable highly-collimated bipolar outflow, and was the first in which kinematically-distinct molecular clumps ('bullets') were detected (Bachiller et al. 1990) at velocities up to 70 km s<sup>−1</sup> from the systemic velocity of the cloud core. SiO 2→1 emission was first detected by Bachiller, Martín-Pintado & Fuente(1991) and mapped in more detail by Dutrey, Guilloteau & Bachiller (1997), so the detection of the 5→4 line was not unexpected. Chernin (1995) discovered water maser emission within the confines of the flow.

A single spectrum was recorded at the position of the millimetre source and is shown in Figure 5. The SiO 5→4 line is detected with a peak antenna temperature ( $T_A^*$ ) of 0.25 K and a gaussian fit to the line yields a linewidth of 15 km s<sup>−1</sup> centered at an LSR velocity of 64 km s<sup>−1</sup>. The most notable aspect to this detection is its large redshift of 55 km s<sup>−1</sup> with respect to the systemic velocity. This is in good agreement with the interferometer maps of Dutrey et al. (1997) which show an SiO peak close to L 1448-mm over an LSR velocity range of 50–75 km s<sup>−1</sup>.

### 3.5. V380 Ori-NE

The outflow from V380 Ori-NE is orientated roughly north-south and displays a high degree of collimation (Davis et al. 2000). Although classified as a class I source by Zavagno et al. (1997), it shares some characteristics with class 0 sources (such as a highly collimated outflow) and may be a transitional object. The SiO spectra in Fig. 6 are from the positions of the CO peaks B1 and R1 (in the nomenclature of Davis et al. 2000). Like the CO 4→3 emission, the SiO line towards B1 is brighter than towards R1. The SiO detection at B1 is also broader than that at R1 (9.9 km s<sup>−1</sup> compared with 6.3 km s<sup>−1</sup>). These positions are also where the H<sub>2</sub> jet curves round, possibly in an interaction with the core in which the driving source is still embedded, although the jet bending may be due to precession of the central source (Davis et al. 2000). However, the observation of SiO emission at these same positions supports the interaction interpretation.

### 3.6. NGC 2071

NGC 2071 is a well-known intermediate-luminosity ( $\sim 500 L_\odot$ ) star-forming region which has long been known to exhibit SiO emission (Chernin & Masson 1993; Garay, Mardones & Rodríguez 2000) in its CO outflow (Moriarty-Schieven, Snell & Hughes 1989). NGC 2071 also houses a cluster of water masers which appear to delineate a compact jet-like feature in the outflow (Torrelles et al. 1998). The 2→1 and 3→2 SiO emission follows the outflow, tracing two lobes which peak 40 arcsec either side of the exciting source.

A single SiO 5→4 spectrum was recorded at the position of the outflow driving source, NGC 2071-IR. The line is detected at an LSR velocity of 2.5 km s<sup>−1</sup>, blueshifted with respect to the systemic velocity. A gaussian fit yields a peak  $T_A^*$  of 0.25 K and a FWHM of 7.1 km s<sup>−1</sup>.

### 3.7. NGC 2024-FIR6

The very compact and high-velocity outflow from NGC 2024-FIR6 was discovered by Richer (1990). FIR6 is the site of a dust continuum peak (Mezger et al. 1988; Visser et al. 1998) and houses a moderately luminous young stellar object, estimated at  $3000 L_{\odot}$ , and is the site of a water maser. Our SiO spectrum shows a tentative detection ( $3\sigma$  peak,  $4\sigma$  in integrated intensity) at an LSR velocity of  $-7.2 \text{ km s}^{-1}$ . This suggests an association with the very high-velocity blue lobe of the FIR6 outflow.

### 3.8. Non-detections

Of the remaining sources, none was detected at a level of  $3\sigma$  or greater. Table 1 lists the peak integrated intensities and main-beam brightness temperatures for the detected sources, while upper limits are given for the non-detections. The upper limits to the brightness temperature are derived from the mean noise level per 2.5-MHz channel in the maps made of each source. The upper limits to the integrated intensity are estimated by integrating the noise per channel over a velocity interval of  $12 \text{ km s}^{-1}$ , which represents the mean velocity extent of the detected sources.

Some of our non-detections are surprising given that a significant number have well-defined outflows and jets. For example, HH 7–11 has a dense component to its outflow, seen in CS and HCO<sup>+</sup> (Rudolph et al. 2001; Rudolph & Welch 1988). The extensive SiO map made by Codella et al. (1999) verifies that the main HH 7–11 flow has no SiO emission along the axis, but does appear to be bounded by a cavity defined by emission from the lower energy 2→1 line. Codella et al. did not detect this component in the 5→4 line. However, the nearby source SVS13B (which we did not cover in our mapping) does show strong 5→4 emission while the 2→1 traces a jet-like outflow (Bachiller et al. 1998).

Cep E was detected by Lefloch, Eislöffel & Lazareff (1996) in the 3→2 line of SiO with a velocity spread of  $30 \text{ km s}^{-1}$ . The non-detection of the 5→4 line indicates that the density within the JCMT beam is probably not high enough to sufficiently excite this line.

Other notable non-detections are HH 24MMS, NGC 2024-FIR5 (30 arcsec north-west of FIR6 and the source of a highly-collimated CO flow: Richer, Hills & Padman 1992), RNO 43 (with its 5-pc long CO flow: Bence et al. 1996) and HH 111 which shows evidence of molecular ‘bullets’ (like L1448-mm: see above) in addition to a well-defined outflow cavity (Nagar et al. 1997; Hatchell, Fuller & Ladd 1999). Possible reasons for the non-detection of SiO towards these sources are discussed in section 5.

## 4. ANALYSIS

In this section we calculate SiO column densities from the observed spectra under the assumption that the lines are optically thin, and that the level populations are in local thermodynamic equilibrium (LTE) which can be characterized by a single temperature. The SiO emission probably arises from regions much smaller than the JCMT beam and so we use main-beam brightness temperatures in our calculations. We also carry out radiative transfer analysis of the emission from HH 25MMS and HH 212 and summarize this in a following subsection.

### 4.1. LTE column densities and abundances

The calculation of beam-averaged SiO column densities employed the following formula, adapted from Irvine et al. (1987):

$$N_{\text{SiO}} = 2.5 \times 10^{12} \int T_{\text{mb}} dv \quad (1)$$

The column density,  $N_{\text{SiO}}$ , is in  $\text{cm}^{-2}$  and the integrated intensity,  $\int T_{\text{mb}} dv$ , is in  $\text{K km s}^{-1}$ . A dipole moment of 3.1 D has been assumed (Ziurys et al. 1989). The fact that we have only a single transition for most sources and that the SiO excitation temperature is not known means that the column densities we derive are strict lower limits if we assume an excitation temperature equal to the energy of the upper level (Macdonald et al. 1996). The  $J=5$  level lies 31 K above the ground state; at this temperature, the fraction of SiO molecules in the  $J=5$  level is 0.133. Table 3 lists the SiO column densities for sources with detected SiO 5→4 emission.

For comparison, CO column densities have also been calculated, and here the choice of velocity range over which to integrate has been chosen to match that of the SiO as closely as possible. In the case of HH 212, for example, both the CO and SiO display redshifted emission and thus it is simply a case of integrating over the same velocity range for each line. For HH 25MMS the SiO emission tends to lie at the systemic velocity while the CO shows both red- and blueshifted components. Since the SiO is clearly spatially associated with the high-velocity gas, it would be incorrect to integrate the CO over the line center. Our approach has been to calculate the ratio of red-shifted SiO to red-shifted high-velocity CO. Finally a beam-averaged abundance relative to molecular hydrogen is also presented in Table 3, where we have assumed that the CO/H<sub>2</sub> ratio is  $10^{-4}$ .

The ratios presented in Table 3 should clearly be treated with some degree of caution, especially as both numerator and denominator are lower limits. A major source of uncertainty is the unknown beam-filling factor of the SiO emission, likely to be significantly lower than the CO (e.g. Chandler & Richer 2001; Dutrey et al. 1997). Allowing for this would increase the SiO column density relative to the CO and thus raise the derived SiO abundance. Another source of uncertainty in the calculations is the choice of excitation temperature. For example, Chandler & Richer (2001) derived values of 150–200 K for HH 211. The fractional population of the respective upper levels for both CO and SiO changes by less than a factor of 3 in the range 30 to 200 K. Assuming the CO and SiO emission arises from the same region leads to higher column densities for each but unchanged abundances. In reality the CO emission is probably more widespread (and thus has a lower mean excitation temperature) than the SiO, so the CO column density *within the SiO-emitting region* is likely to be lower than listed in Table 3. Therefore the SiO abundance is probably higher than given in Table 3.

### 4.2. Radiative transfer modeling

In addition to the LTE analysis, for HH 25MMS and HH 212 we have data in more than one transition and thus have attempted to further constrain the properties of the shocked gas with a statistical equilibrium code employing the large velocity gradient (LVG) approximation

(Goldreich & Kwan 1974). Collision rates were taken from Turner et al. (1992). The parameter space covered by the modeling extends from a density of  $10^4 \text{ cm}^{-3}$  to  $10^9 \text{ cm}^{-3}$ , a temperature of 20 to 150 K and an abundance of SiO from  $10^{-11}$  to  $10^{-7}$  relative to H<sub>2</sub>. The velocity gradient was assumed to be the FWHM linewidth of the SiO line divided by the beam diameter. Since the emitting regions are likely to be much smaller than the beam, fitting the line brightnesses produced solutions with low beam-averaged abundances, lower than derived from the LTE analysis in the previous section. Since the line ratios constrain the density fairly well while being only weakly dependent on temperature, the only parameter which is likely to be in error is the SiO abundance. The solutions for each source are described in more detail below and are presented graphically in Fig. 9.

#### 4.2.1. HH 25MMS

At the location of the CO peak in HH 25MMS we have long-integration spectra of the 5→4 and 8→7 transitions, plus a lower-sensitivity 7→6 spectrum (see Fig. 3). Table 4 lists the relevant parameters of these lines.

The results are not particularly well constrained and no single solution could be obtained. The range of acceptable solutions required a kinetic temperature 50–100 K, an SiO abundance of  $2\text{--}20 \times 10^{-11}$  and a density of order  $10^6 \text{ cm}^{-3}$ . Higher abundance solutions were ruled out on the basis that the line ratio required a higher density solution compared with the observed line intensities. Fig. 9a shows a typical solution for a temperature of 100 K.

It is interesting to compare these results with those derived for methanol at the same position by GD98. In this case, a temperature of about 60 K gave the best fit as well as a lower density than for the SiO ( $1\text{--}4 \times 10^5 \text{ cm}^{-3}$ ). This perhaps begins to provide a picture of how the various molecules are distributed in shocked gas: the SiO lies in the higher density gas, immediately post-shock while molecules such as methanol exist in a lower density environment. Higher-resolution observations are critical to testing this hypothesis.

#### 4.2.2. HH 212

Chapman et al. (2002) report the detection of SiO 2→1 emission close to the location of driving source of the HH 212 jet. They detect two velocity components, in good agreement with our 5→4 detections shown in Figure 4 suggesting that they are tracing the same components that we detect in the 5→4 line. Table 4 summarizes the results of the LVG modeling. Similar solutions are found for each position, although the temperature is slightly better constrained for the SW position at  $(-8, -18)$ . The density in the SiO-emitting region is of order  $10^5 \text{ cm}^{-3}$  and the beam-averaged SiO abundance is estimated to be a few times  $10^{-9}$ . Fig. 9b shows a typical solution for a temperature of 100 K.

#### 4.3. LVG modeling discussion

Interpreting the results of the LVG modeling is not necessarily straightforward, so here we elaborate on the meaning of the results. The LVG approximation assumes a constant velocity gradient across the clump of molecular gas.

In addition, in our modeling, the clump has constant kinetic temperature and density. For a set of inputs (line brightness temperatures and ratios) the LVG code predicts the brightness temperature of each SiO transition for a range of densities, temperatures and abundances. Since the temperature and density are assumed to be constant, the same is true for the abundance.

In practice the effective output abundance,  $X$ , is the abundance divided by the velocity gradient,  $dv/dr$ , i.e.  $X/(dv/dr)$  (see Goldreich & Kwan 1974). Thus models may be run for one value of  $dv/dr$  and solutions for the abundance may be scaled to other possible values of  $dv/dr$ . Furthermore, if the emission arises from a region much smaller than the beam, then the true abundance is higher since  $X/(dv/dr)$  is constant. Thus the abundances we derive from LVG modeling are lower limits. In the optically thin limit, a high-density/low-abundance solution is qualitatively the same as a low-density/high-abundance solution.

Since there are three parameters being solved for, three input values are necessary. Ideally three independent values are desirable (i.e. three different transitions), but in our case we use the two line brightness temperatures and their ratio.

The solutions given in Table 4 yield abundances for SiO that are lower than the LTE values derived in Section 4.1. While the observed line ratios do not rule out higher abundances, the observed line *intensities* do: higher abundance solutions predict higher line intensities. Therefore, if the true abundance of SiO is higher than that predicted by the LVG modeling, then the observed line intensities must be low as a result of beam dilution. In section 5.2.3 below, we estimate that the filling factor for the 5→4 emission probably lies between 0.01 and 0.2. If we take the (geometric) mean and correct the observed line intensities accordingly (assuming that all the lines are equally affected) then the LVG models predict solutions with a higher abundance than without the correction applied. This is shown by the ‘Corrected’ curves in Fig. 9c and d. The increase in the abundance is roughly proportional to the reciprocal of the filling factor since the SiO emission in the models is optically thin.

## 5. DISCUSSION

In this section we will discuss our results and investigate possible reasons for the lack of widespread SiO 5→4 emission towards our sample of outflow sources. Note that this discussion is biased toward understanding the factors influencing only the detection of the 5→4 line. As shown by Codella et al. (1999), lower-lying transitions may trace different excitation conditions to which the 5→4 line is not sensitive.

To recap on the results presented above, of 25 outflow sources observed, SiO 5→4 emission was detected in only 7, a 28 per cent detection rate. From these data there is weak evidence for a correlation between the evolutionary status of the outflow driving source and SiO emission: 5 out of 7 of the detected sources satisfy the class 0 criteria and are presumably relatively young. The results from the LVG modeling suggest that the molecular hydrogen density in the SiO-emitting regions is of order  $10^5\text{--}10^6 \text{ cm}^{-3}$ .

### 5.1. Which sources show SiO emission?

Here we examine a number of potential correlations between source properties and SiO emission in order to assess whether or not these parameters play a role in determining the strength of SiO emission. The first correlations to examine are the obvious ones involving outflow velocity and power. Values for the outflow parameters have been taken from the literature where possible. In the cases where none has been published, then we have assumed that the mean velocity is half the maximum velocity and the mean radius is half the maximum radius of the outflow (where the lobes are of unequal size, an average of those values was used). In addition we have calculated the outflow parameters in the following way. The dynamical timescale for the outflow,  $t_{\text{dyn}} = 9.8 \times 10^5 r/v$  years, where the radius,  $r$ , is in pc and the velocity  $v$  is in  $\text{km s}^{-1}$ , the momentum flux,  $\dot{p} = Mv/t_{\text{dyn}} \text{M}_\odot \text{km s}^{-1} \text{yr}^{-1}$ , where  $M$  is the outflow mass in  $\text{M}_\odot$ , and the mechanical luminosity  $L_{\text{mech}} = 81\dot{p}v \text{L}_\odot$ .

In our attempt to understand the processes which give rise to detectable SiO emission, we examine possible correlations between the observed SiO emission and a number of source properties. Since SiO is formed in shocked gas, it is reasonable to search for correlations between the SiO emission and outflow properties, such as the velocity, outflow force and mechanical luminosity. These properties all likely reflect the driving source (stellar) luminosity, so we do not separately plot this quantity. Since the SiO lines require high densities to excite, another property which may influence the SiO emission is the density of the medium through which the outflow is propagating.

Figure 10 shows the SiO  $5\rightarrow4$  luminosity (in units of  $\text{L}_\odot$ ) plotted against five source properties: the maximum velocity in the outflow,  $V_{\text{max}}$ , the outflow force, mechanical luminosity, number density of  $\text{H}_2$  derived from the submillimetre continuum emission (or the ‘submillimetre density’: see section 5.2.2 below) and source bolometric luminosity. Note that we only include data for the sources which lie in the distance range 330 to 450 pc (see section 5.2.5 below). In estimating the density, we have assumed that the emission comes from a region 15 arcsec in diameter (equal to the JCMT beam at 850  $\mu\text{m}$ ) and have used published dust temperatures where available. The precise emissivity used is not important because we are only interested in relative differences between the sources and we assume that the emissivity is the same for all the sources in our sample.

No clear correlations are observed between SiO emission and any of the plotted properties, although Fig. 10 does suggest that sources with faster outflows are more likely to exhibit SiO emission, and there is a weak trend that sources with higher ambient gas densities are also more likely to be detected in our survey (see the following section for more detailed discussion). Contrary to the results of Codella et al. (1999; Fig. 10e) we find no unambiguous correlation between source luminosity and strength of SiO emission. However, it should be noted that the Codella et al. sample includes higher luminosity sources, and includes only one young, low-mass, class 0 source (SVS13B). Since we conclude below that SiO is a good indicator of such objects, it is perhaps not surprising that we do not observe any correlation. The Codella et al. observation

that the more luminous sources exhibit stronger SiO emission can in fact be explained by the same conclusion we reach, namely that the ambient density plays some role in determining the presence of SiO emission.

### 5.2. Factors influencing SiO production and excitation

#### 5.2.1. Shock velocity

The shock velocity needed to disrupt dust grains sufficiently to release Si from grain mantles into the gas phase is of order  $25 \text{ km s}^{-1}$  (Schilke et al. 1997). Most of our SiO detections are from outflows with (line-of-sight) velocities exceeding  $20 \text{ km s}^{-1}$ . If projection effects are taken into account, then it is likely that all the SiO detected-flows have velocities greater than  $20 \text{ km s}^{-1}$  (e.g. the HH 25MMS flow probably lies within 20 degrees of the plane of the sky, leading to a corrected flow velocity of at least  $24 \text{ km s}^{-1}$ : see GD98). The majority of sources in our sample, however, have  $V_{\text{max}}$  below this value. There is no clear correlation between SiO line strength and maximum outflow velocity although this is probably because there are other factors which determine the intensity of SiO emission (and these are discussed below). However, of the outflow sources with maximum (line-of-sight) velocities greater than  $20 \text{ km s}^{-1}$ , almost half of them exhibit SiO emission. In this sample, on average, the outflows with SiO emission have higher CO velocities than those without ( $30 \text{ km s}^{-1}$  compared with  $15 \text{ km s}^{-1}$ ). Therefore, as one might expect, the outflow velocity does appear to play some role in determining the degree of SiO emission.

#### 5.2.2. Density

A high shock velocity alone is probably insufficient to lead to strong SiO emission: the density must also be a factor. The critical density for the excitation of the  $5\rightarrow4$  line of SiO is of order  $5\text{--}10 \times 10^6 \text{ cm}^{-3}$ . (Those for the  $7\rightarrow6$  and  $8\rightarrow7$  lines are more than a factor of ten higher.) Therefore in order for this line to be detected in our survey, either the gas must be very hot for beam dilution not to render the line undetectable, or the mean density across a 22-arcsec diameter beam must be at least a few times  $10^6 \text{ cm}^{-3}$ . Our LVG results (above) confirm that in those sources which are detected in SiO emission, the density is indeed probably close to this value, and in the case of HH 25MMS that the higher transitions are not thermalized.

Of course, the SiO emission originates in the post-shock gas, so the densities derived above refer to this component. The compression ratio for a C-shock is of order  $\sqrt{2}$  times the magnetic Mach number (shock speed divided by the Alfvén velocity: e.g. Spitzer 1978). For a shock velocity of  $25 \text{ km s}^{-1}$  and an Alfvén velocity of  $1.5\text{--}2.5 \text{ km s}^{-1}$  (estimated from the linewidths of ambient gas tracers), the compression in a C-shock is of order 15–25 (as borne out by models of shocks: e.g. Wardle 1991). Therefore, in order for the post-shock gas to reach densities of order  $5 \times 10^6 \text{ cm}^{-3}$ , then the pre-shock density needs to be at least  $2 \times 10^5 \text{ cm}^{-3}$ , a somewhat less stringent limit but still higher than the typical density of low-mass dense cloud cores, such as those traced by ammonia (Benson & Myers 1989). Therefore it seems reasonable to expect that higher density regions are favoured for the production of SiO  $5\rightarrow4$  emission.

As a way of exploring whether the density of the *ambient* gas plays a role in determining the strength of the SiO emission, we have plotted the SiO luminosity against the submillimetre density, a quantity designed to represent the mean ambient density within a 15-arcsec beam in Figure 10. As in the case for the maximum velocity, there is no clear trend but on average it does appear from this crude analysis that the sources which show SiO emission lie in regions with higher densities than those which are not detected.

### 5.2.3. Incomplete beam-filling

From the LVG analysis it is evident that the SiO lines in HH 25MMS originate from unresolved components within a 15-arcsec beam because the solutions for the line ratios predict higher abundances than the line intensities. To bring the solutions into agreement we can assume the emission fills a small fraction of the beam and scale the line brightnesses to derive a consistent solution. Using this approach it is possible to estimate that the lines have beam-filling factors of order 0.01 to 0.2. These filling factors correspond to source diameters in the range 1.5 to 7 arcsec, and are in good agreement with estimates in other sources (e.g. Avery & Chiao 1996). Such size scales are comfortably within the range of current interferometers and a future test would be to observe the detected outflow sources with arcsecond resolution. The VLA study of HH 211 by Chandler & Richer (2001) show that this estimate is not unreasonable.

### 5.2.4. Chemistry in shocked gas

While the abundance of SiO is enhanced by the action of the shock, the density may be sufficiently high such that the depletion timescale becomes shorter than the shock crossing timescale, thus ‘quenching’ emission from SiO by lowering the abundance. Such conditions may be met in very dense regions and where the post-shock gas quickly cools to 100 K or less at which point the SiO can then freeze out onto the dust grains. From the models of Schilke et al. (1997), the shock crossing time is calculated to be 20000 years for a shock speed of 25 km s<sup>-1</sup>. The depletion timescale is  $2 \times 10^9 / n_{\text{H}_2}$  years (where  $n_{\text{H}_2}$  is the molecular hydrogen number density in cm<sup>-3</sup>). These two values are equal when the density is 10<sup>5</sup> cm<sup>-3</sup>, marginally lower than the post-shock densities inferred above. This may account for the non-detection of SiO towards high ambient density sources such as HH 24MMS and NGC 2024-FIR5.

Another mechanism for removing SiO from the gas phase (once formed) is for it to pass through a second shock in which reactions with OH (abundance in shocks) rapidly form SiO<sub>2</sub>. Schilke et al. (1997) demonstrate in their shock models that a region where SiO is the dominant pre-shock reservoir for silicon will have a lower maximum abundance of SiO (by up to an order of magnitude) compared with those regions where Si is in other forms.

### 5.2.5. Spatial coverage and sensitivity

We have considered whether the non-detections in our survey result from mapping an insufficiently large area. Our mapping scheme involved two approaches: a grid of points covering the outflow source and its environment (for small outflows), and strip maps (for large outflows) where

spectra were recorded at beamwidth spacing covering the extent of the known CO outflow. In the latter case, if SiO emission was detected along this axis then the mapping was extended to cover off-axis points (time permitting). In one case (RNO43-mm) the flow was too large to cover completely so the mapping focused on the region close to the driving source and the positions of the known CO and/or H $\alpha$  peaks. It is worth noting that for sources where off-axis SiO emission was detected, emission *on* the outflow axis was detected as well. Examining the SiO detections from other low-mass outflow sources in the literature (see Section 5.3) we note that in all cases, an on-axis strip-map with a 22-arcsec beam would have detected the SiO emission. We therefore conclude that poor spatial coverage is not a contributing factor to our non-detections.

We also consider whether the range in sensitivity of the SiO measurements could give rise to the apparent lack of correlation between SiO luminosity and source properties. With the exception of Cep E, L1660 and NGC2264G, all of our sources lie within 500 pc; furthermore 80 per cent lie within the range 330 to 450 pc. On average, the range of noise levels ( $\Delta T_{\text{mb}}$ ) in our data is within 26 per cent of 105 mK (although there are a couple of sources with somewhat higher levels). Considering just the subsample of 20 sources which lie between 330 and 450 pc the sensitivity is uniform to within 34 per cent, assuming the dispersions in the noise level and distance add in quadrature. The lack of correlation observed in Figure 10a-d is therefore an intrinsic property of these data and we conclude that our sensitivity is not a significant contributing factor.

## 5.3. SiO emission from other low-mass sources

A handful of other low-mass protostars are known to exhibit SiO emission. These include IRAS 16293–2422 (Castets et al. 2001; Blake et al. 1994), NGC1333–IRAS4 (Blake et al. 1995; Lefloch et al. 1998), BHR 71 (Garay et al. 1998), L 1157 (Avery & Chiao 1996; Bachiller et al. 2001), B1 (Yamamoto et al. 1992) and SVS13B (Bachiller et al. 1998). While the evolutionary statuses of B1 and SVS13B are not well determined, the others are well-known class 0 protostars. This fact lends further support to our conclusion above that the density of the circumstellar environment plays an important role in determining the level of SiO emission.

## 5.4. Water masers and SiO emission

Recent surveys have detected a sample of low luminosity objects which exhibit water maser emission (Claussen et al. 1996; Furuya et al. 2001, 2003). Four of the seven SiO sources in our sample are water maser sources – L 1448-mm, NGC2024-FIR6, NGC 2071 and HH 212. In addition three further objects have water masers but no SiO emission – RNO15FIR, HH 7–11 and Cep E, although HH 7–11 and Cep E have been detected in lower-lying transitions of SiO (see section 3.8 above). In addition, of the known SiO sources that we did not observe in this sample, three (IRAS 16293-2422, NGC1333-IRAS4 and L 1157) have water masers associated with them. Furuya et al. (2001) concluded that class 0 sources are more likely to have water masers than more evolved sources, and suggest that this is because there is a larger quantity of dense gas in these sources. Although the statistics are poor, the results of

our survey suggest that sources which exhibit water maser emission may also be likely to show SiO emission.

Harju et al. (1998) searched for SiO emission towards water maser sources covering a wide range of luminosities. For the range of luminosities covered by our sample, they find a similar detection rate ( $\sim 20$  per cent). We also note that the detection rate for more luminous sources increases rapidly to  $\sim 50$  per cent, probably reflecting the higher temperatures and densities in these regions.

### 5.5. Summary

In practice, these factors (shock velocity, density and incomplete beam-filling) all contribute to determining whether a source exhibits SiO emission. Nearby sources will suffer obviously less from incomplete beam-filling, which may explain why we do not detect Cep E, NGC 2264G or L 1660. Shock velocity and density are probably linked as class 0 sources are found in the highest density environments, and are observed to have the most powerful flows, while many also have very high-velocity outflows. Therefore, it seems reasonable to conclude that class 0 sources are those most likely to exhibit SiO emission, and as such that SiO emission (like water masers) may be used as a (statistical) signpost for the presence of a very young, protostellar candidate.

## 6. CONCLUSION

We have observed the SiO  $J=5\rightarrow4$  line towards a sample of 25 low-luminosity ( $L_* < 10^3 L_\odot$ ) protostellar outflow systems. The line was clearly detected towards 7 of the 25 sources, a detection rate of 28 per cent. The majority (5 out of 7) of sources detected are of class 0 status. We detect a greater fraction of class 0 sources compared with other classes (45 per cent compared with 18 and 0 per cent for class I and II). However, given the small numbers involved, the significance of this result should be regarded as tentative.

In four cases (HH 25MMS, HH 212, V-380 Ori NE and HH 211) emission was detected at positions offset from the

center (in two other cases it is known that SiO emission also occurs away from the central source position). LTE analysis yields SiO abundances ranging from  $10^{-8}$  to as high as  $8\times 10^{-7}$ . In two cases (HH 25MMS and HH 212) we have conducted LVG modeling of the emission, and find that the SiO emission arises in regions with temperatures of typically 30–100 K, densities of  $10^5$  to  $10^6$  cm $^{-3}$  and SiO abundances of  $10^{-11}$  to  $10^{-9}$  relative to H<sub>2</sub>. These abundances are lower than those derived from LTE analysis, a result consistent with the notion that the SiO emission arises in clumps which are much smaller than the 22-arcsec beam. Higher resolution observations has shown this is true, and we feel that further high-resolution studies are desireable in order to determine the conditions of the post-shock gas.

We have explored a number of possible reasons for the detection of SiO in some sources but not others, and conclude that the shock velocity and density of the ambient medium play an important role. We can therefore account for the fact that most of the detected sources have class 0 status. We conclude that while not all class 0 sources exhibit SiO emission, SiO emission is a good signpost for class 0 sources.

The authors would like to thank PPARC for financial support and the JCMT support staff for conducting some of the observations in service mode. AGG was supported by NSF grant AST-9981289 to the University of Maryland for part of this work. AGG wishes to thank Tom Hartquist for helpful discussions on SiO chemistry in shocks, and Nicholas Chapman for communicating results on HH 212. The referee is thanked for useful comments which helped clarify the presentation. The JCMT is operated by the Joint Astronomy Centre on behalf of the UK Particle Physics and Astronomy Research Council, the Netherlands Organization for Scientific Research and the National Research Council of Canada.

## REFERENCES

Avery L.W., Chiao M., 1996, ApJ, 463, 642  
 Bachiller R., Cernicharo J., 1990, A&A, 239, 276  
 Bachiller R., Cernicharo J., Martín-Pintado J., Tafalla M., Lazareff B., 1990, A&A, 231, 174  
 Bachiller R., Martín-Pintado J., Fuente A., 1991, A&A, 243, L21  
 Bachiller R., Guilloteau S., Dutrey A., Planesas P., Martín-Pintado J., 1995, A&A, 299, 857  
 Bachiller R., Guilloteau S., Gueth F., Tafalla M., Dutrey A., Codella C., Castets A., 1998, A&A, 339, L49  
 Bachiller R., Pérez Gutiérrez M., Kumar M.S.N., Tafalla M., 2001, A&A, 372, 899  
 Bence S.J., Richer J.S., Padman R., 1996, MNRAS, 279, 866  
 Benson P.J., Myers P.C., 1989, ApJS, 71, 89  
 Blake G.A., van Dishoeck E.F., Jansen D.J., Groesbeck T.D., Mundy L.G., 1994, ApJ, 428, 680  
 Blake G.A., Sandell G., van Dishoeck E.F., Groesbeck T.D., Mundy L.G., Aspin C., 1995, ApJ, 441, 689  
 Bontemps S., André P., Ward-Thompson D., 1995, A&A, 297, 98  
 Caselli P., Hartquist T.W., Havnes O., 1997, A&A, 322, 296  
 Castets A., Ceccarelli C., Loinard L., Caux E., Lefloch B., 2001, A&A, 375, 40  
 Cernicharo J., Reipurth B., 1996, ApJ, 460, L57  
 Chandler C.J., Richer J.S., 2000, ApJ, 530, 851  
 Chandler C.J., Richer J.S., 2001, ApJ, 555, 139  
 Chapman N.L., Mundy L.G., Lee C.-F., White S.M., 2002, BAAS, 201, 2001  
 Chernin L.M., 1995, ApJ, 440, L97  
 Chernin L.M., 1996, ApJ, 460, 711  
 Chernin L.M., Masson C.R., 1993, ApJ, 403, L21  
 Chernin L.M., Masson C.R., 1995, ApJ, 443, 181  
 Chini R., Krügel E., Haslam C.G.T., Kreysa E., Lemke R., Reipurth B., Sievers A., Ward-Thompson D., 1993, A&A, 272, L5  
 Chini R., Ward-Thompson D., Kirk J.M., Nielbock M., Reipurth B., Sievers A., 2001, A&A, 369, 155  
 Claussen M.J., Marvel K.B., Wootten A., Wilking B.A., 1998, ApJ, 507, L79  
 Claussen M.J., Wilking B.A., Benson P.J., Wootten A., Myers P.C., Terebey S., 1996, ApJS, 106, 111  
 Codella C., Bachiller R., Reipurth B., 1999, A&A, 343, 585  
 Cohen M., Schwartz R.D., 1987, ApJ, 316, 311  
 Davis C.J., Ray T.P., Eislöffel J., Corcoran D., 1997a, A&A, 324, 263  
 Davis C.J., Eislöffel J., Ray T.P., Jenness T., 1997b, A&A, 324, 1013  
 Davis C.J., Dent W.R.F., Matthews H.E., Coulson I.M., McCaughrean M.J., 2000, MNRAS, 318, 952  
 Dutrey A., Guilloteau S., Bachiller R., 1997, A&A, 325, 758  
 Fich M., Lada C.J., 1997, ApJ, 484, L63  
 Furuya R.S., Kitamura Y., Wootten H.A., Claussen M.J., Kawabe R., 2001, ApJ, 559, L143  
 Furuya R.S., Kitamura Y., Wootten H.A., Claussen M.J., Kawabe R., 2003, ApJS, 144, 71  
 Fukui Y., Iwata T., Mizuno A., Bally J., Lane, A.P., 1993, in Levy E.H., Lunine J.I., eds, Protostars and Planets III. Tucson, University of Arizona Press, p. 603  
 Garay G., Köhnenkamp I., Bourke T.L., Rodríguez L.F., Lehtinen K.K., 1998, ApJ, 509, 768

Garay G., Mardones D., Rodríguez L.F., 2000, *ApJ*, 545, 861  
 Gibb A.G., Davis C.J., 1998, *MNRAS*, 298, 644 (GD98)  
 Gibb A.G., Heaton B.D., 1993, *A&A*, 276, 511 (GH93)  
 Goldreich P., Kwan J., 1974, *ApJ*, 189, 441  
 Gueth F., Guilloteau S., 1999, *A&A*, 343, 571  
 Harju J., Lehtinen K.K., Booth R.S., Zinchenko I., 1998, *A&AS*, 132, 211  
 Hatchell J., Fuller G.A., Ladd E.F., 1999, *A&A*, 346, 278  
 Irvine W.M., Goldsmith P.F., Hjalmarson Å., 1987, in *Hollenbach D.J., Thronson H.A., Jr, eds, Interstellar Processes*. Reidel, Dordrecht, p. 561  
 Knee L.B.G., Sandell G., 2000, *A&A*, 361, 671  
 Lada C.J., Fich M., 1996, *ApJ*, 459, 638  
 Ladd E.F., Hodapp K.-W., 1997, *ApJ*, 474, 749  
 Lee C.-F., Mundy L.G., Reipurth B., Ostriker E.C., Stone J.M., 2000, *ApJ*, 542, 925  
 Lefloch B., Eislöffel J., Lazareff B., 1996, *A&A*, 313, L17  
 Lefloch B., Castets A., Cernicharo J., Loinard L., 1998, *ApJ*, 504, L109  
 Looney L.W., Mundy L.G., Welch W.J., 2000, *ApJ*, 529, 477  
 Macdonald G.H., Gibb A.G., Habing H.J., Millar T.J., 1996, *A&AS*, 119, 333  
 Martín-Pintado J., Bachiller R., Fuente A., 1992, *A&A*, 254, 315  
 McCaughrean M.J., Rayner J.T., Zinnecker H., 1994, *ApJ*, 436, L189  
 Meehan L.S.G., Wilking B.A., Claussen M.J., Mundy L.G., Wootten A., 1998, *AJ*, 115, 1599  
 Mezger P.G., Chini R., Kreysa E., Wink J.E., Salter C.J., 1988 *A&A*, 191, 44  
 Mitchell G.F., Hasegawa T.I., Dent W.R.F., Matthews H.E., 1994, *ApJ*, 436, L177  
 Mitchell G.F., Johnstone, D., Moriarty-Schieven, G., Fich, M., Tothill, N.F.H., 2001, *ApJ*, 556, 215  
 Monin J.-L., Pudritz R.E., Lazareff B., 1996, *A&A*, 305, 572  
 Moriarty-Schieven G.H., Snell R.L., Hughes V.A., 1989, *ApJ*, 347, 358  
 Moro-Martín A., Cernicharo J., Noriega-Crespo A., Martín-Pintado J., 1999, *ApJ*, 520, L111  
 Nagar N.M., Vogel S.N., Stone J.M., Ostriker E.C., 1997, *ApJ*, 482, L195  
 Nisini B., Codella C., Giannini T., Richer J.S., 2002, *A&A*, 395, L25  
 Phillips R.R., Gibb A.G., Little L.T., 2001, *MNRAS*, 326, 927  
 Reipurth B., Olberg M., 1991, *A&A*, 246, 535  
 Richer J.S., 1990, *MNRAS*, 245, 24P  
 Richer J.S., Hills R.E., Padman R., 1992, *MNRAS*, 254, 525  
 Rudolph A.L., Bachiller R., Rieu N.Q., Van Trung D., Palmer P., Welch W.J., 2001, *ApJ*, 558, 204  
 Rudolph A.L., Welch W.J., 1988, *ApJ*, 326, L31  
 Sandell G., Knee L.B.G., Aspin C., Robson E.I., Russell A.P.G., 1994, *A&A*, 285, L1  
 Schilke P., Walmsley C.M., Pineau des Forêts G., Flower D.R., 1997, *A&A*, 321, 293  
 Schwartz P.R., Gee G., Huang Y.-L., 1988, *ApJ*, 327, 350  
 Shirley Y.L., Evans N.J., II, Rawlings J.M.C., Gregersen E.M., 2000, *ApJS*, 131, 249  
 Spitzer L., 1978, *Physical Processes in the Interstellar Medium*. Wiley, New York, p. 221-222.  
 Stapelfeldt K.R., Scoville N.Z., 1993, *ApJ*, 408, 239  
 Torrelles J.M., Gómez J.F., Rodríguez L.F., Curiel S., Anglada G., Ho P.T.P., 1998, *ApJ*, 505, 756  
 Turner B.E., Chan K.-W., Green S., Lubowich D.A., 1992, *ApJ*, 399, 114  
 Visser A.E., Richer J.S., Chandler C.J., Padman R., 1998, *MNRAS*, 301, 585  
 Ward-Thompson D., Eiroa C., Casali M.M., 1995, *MNRAS*, 273, L25  
 Wardle M., 1991, *MNRAS*, 250, 253  
 Wu Y., Huang M., He J., *A&AS*, 1996, 115, 283  
 Yamamoto S., Mikami H., Saito S., Kaifu N., Ohishi M., Kawaguchi K., 1992, *PASJ*, 44, 459  
 Yu K.C., Billawalla Y., Bally J., 1999, *AJ*, 118, 2940  
 Zavagno A., Molinari S., Tommasi E., Saraceno P., Griffin M.J., 1997, *A&A*, 325, 685  
 Zinnecker H., Bastien P., Arcoragi J.-P., Yorke H.W., 1992, *A&A*, 265, 726  
 Zinnecker H., McCaughrean M.J., Rayner J.T., 1998, *Nature*, 394, 862  
 Ziurys L.M., Friberg P., Irvine W.M., 1989, *ApJ*, 343, 201

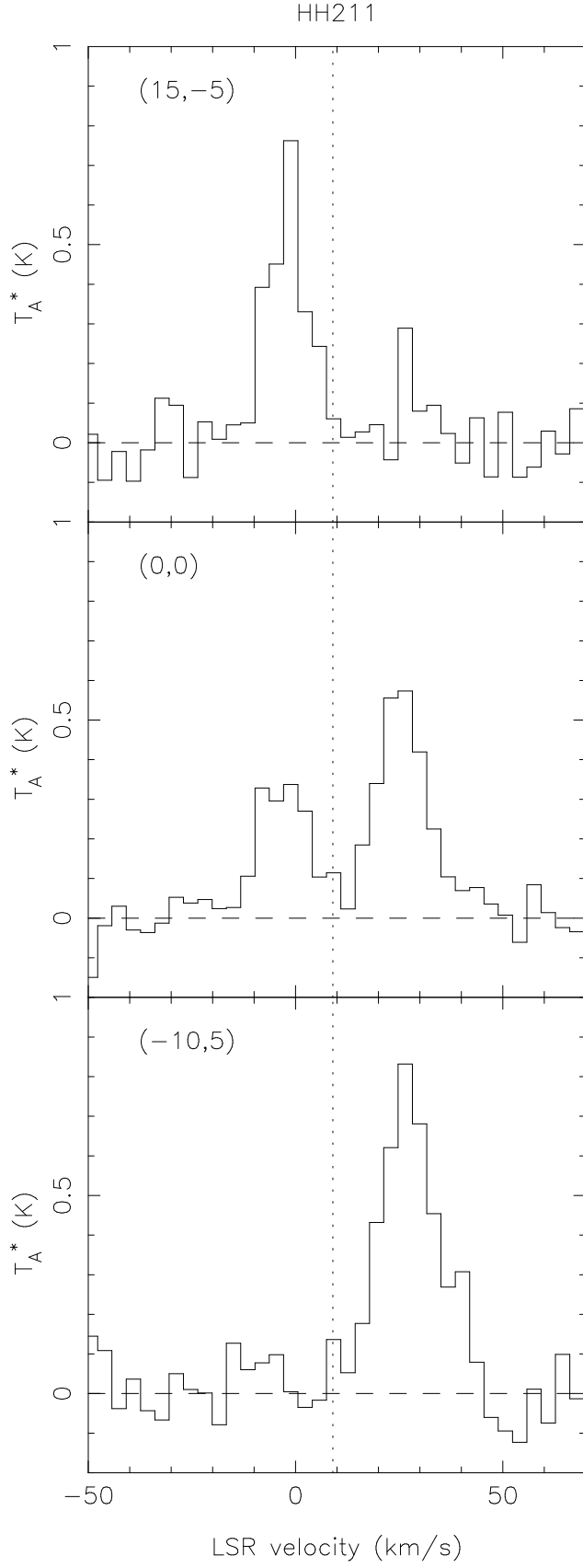


FIG. 1.— SiO 5→4 spectra towards three positions in the HH 211 outflow. Top: from the blue lobe; Center: at the source position; Bottom: red lobe. The vertical dotted line marks the LSR velocity.

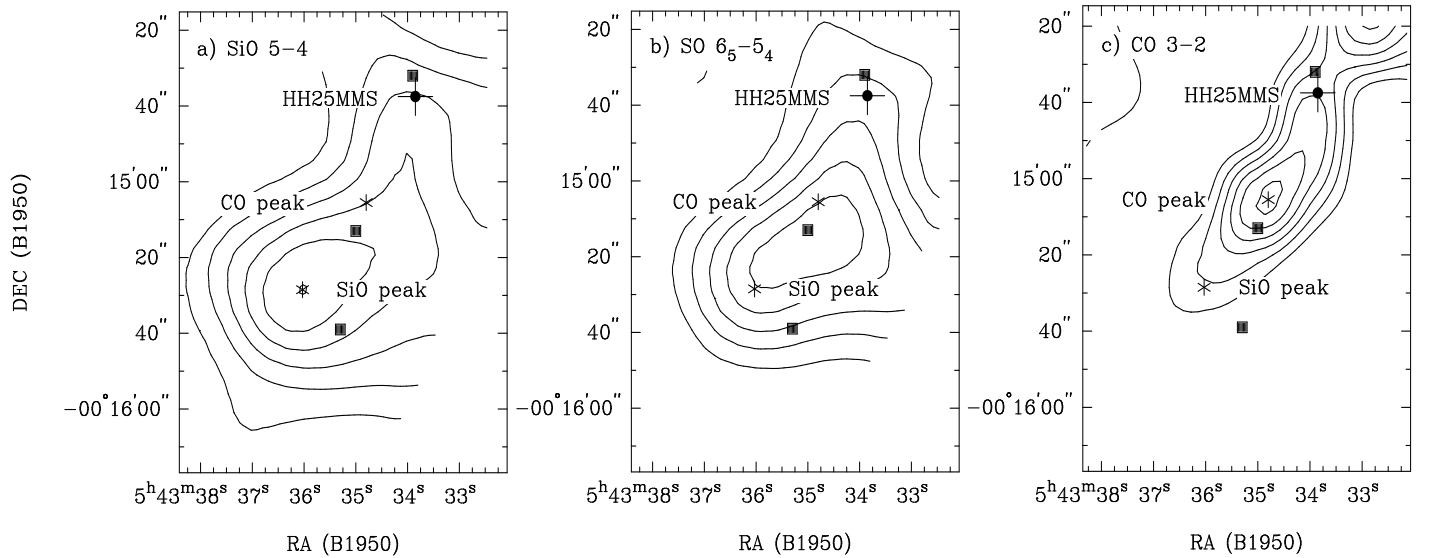


FIG. 2.— a) SiO 5→4 integrated intensity in the range 8 to 15  $\text{km s}^{-1}$ . b) SO 6<sub>5</sub>→5<sub>4</sub> integrated intensity in the range 8 to 12  $\text{km s}^{-1}$ . c) Redshifted CO 3→2 emission from the HH 25MMS outflow for comparison (Fig. 1a from GD98). In all three panels, the position of HH 25MMS is marked by a cross and filled circle, the knots comprising HH25 as open squares and the SiO and CO peaks by asterisks.

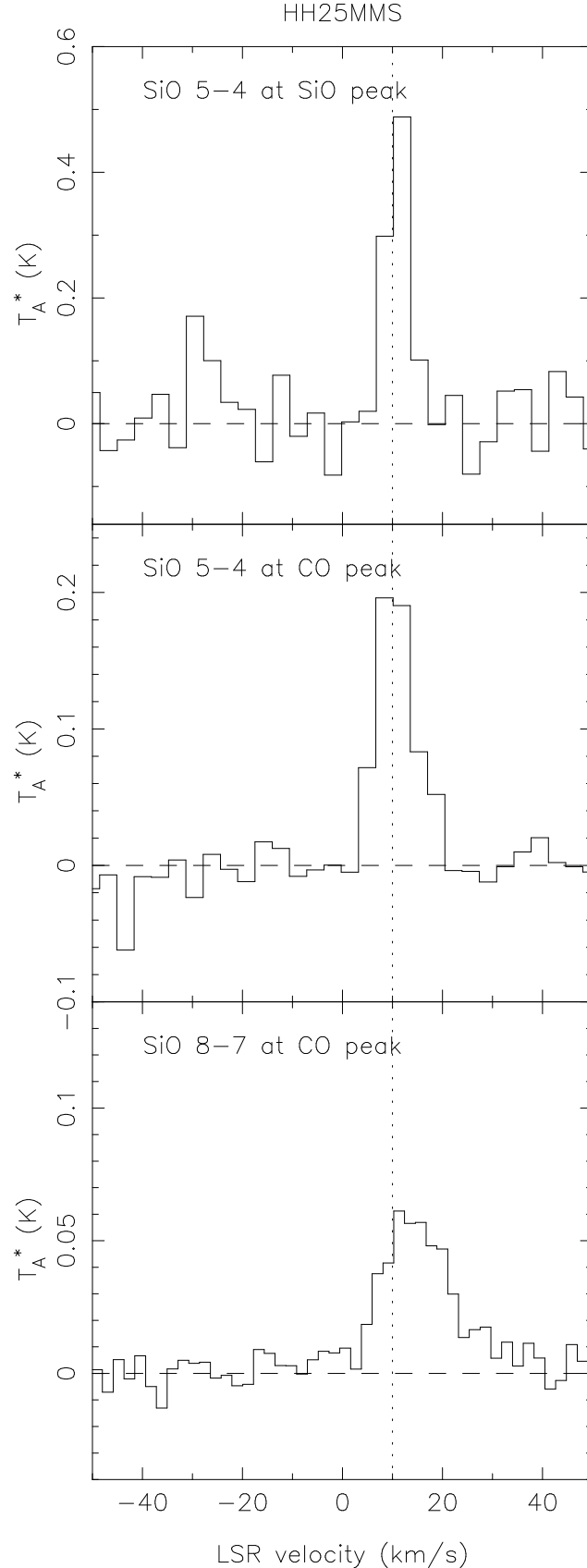


FIG. 3.— Top: SiO 5→4 spectrum towards the SiO peak. Center: SiO 5→4 spectrum towards the CO peak. Bottom: SiO 8→7 spectrum towards the CO peak. The noise levels are 52, 20 and 6 mK per 2.5-MHz channel respectively. The vertical dotted line marks the LSR velocity.

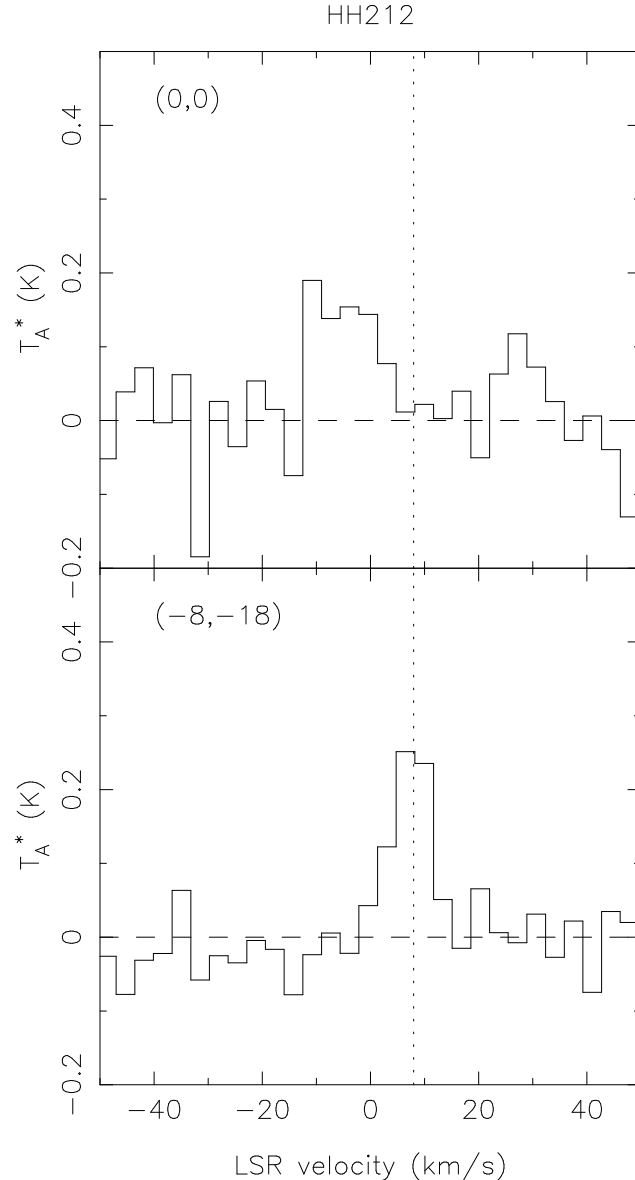


FIG. 4.—Top: SiO 5→4 line towards the central position in HH 212, and Bottom: towards  $(-8, -18)$  arcsec offset. The line shown peaks at  $-6.0 \text{ km s}^{-1}$  and has a width of  $\sim 16 \text{ km s}^{-1}$ . Note that in the top panel there may be redshifted counterpart to the highly blueshifted line, peaking close to  $28 \text{ km s}^{-1}$ . However, this peak is only detected at the  $2\sigma$  level. The vertical dotted line marks the LSR velocity.

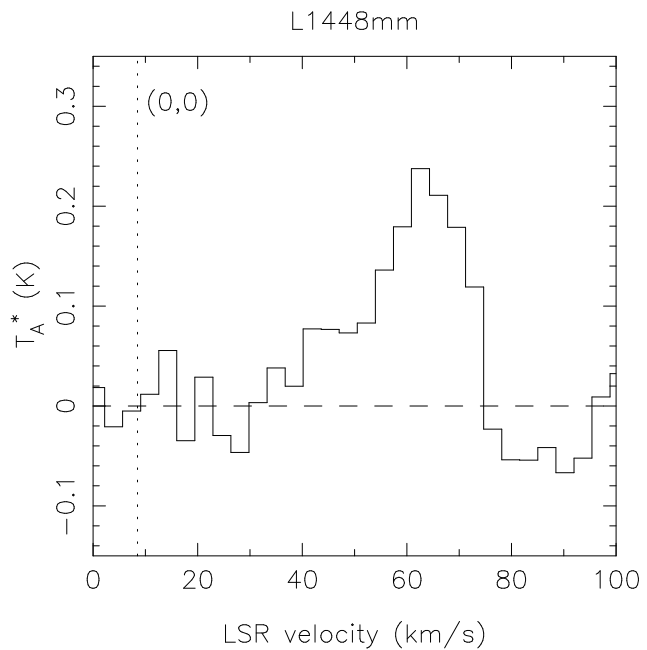


FIG. 5.— SiO 5→4 spectra towards the L 1448 outflow. The vertical dotted line marks the LSR velocity.

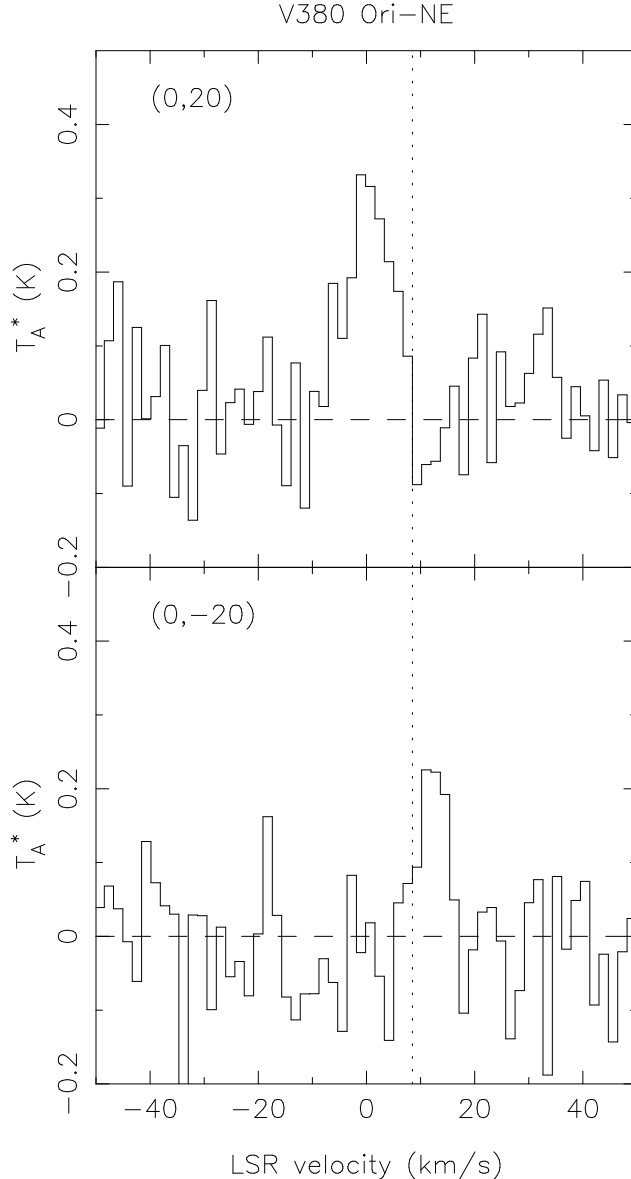


FIG. 6.— SiO 5→4 spectra towards the positions B1 and R1 (in the nomenclature of Davis et al. 2000) in the outflow from V380 Ori-NE. Top: 20 arcsec north of center (B1), and Bottom: 20 arcsec south (R1). Note that the line towards B1 is blueshifted by nearly  $10 \text{ km s}^{-1}$  relative to the systemic velocity, while that towards R1 is only slightly redshifted ( $+2.2 \text{ km s}^{-1}$ ). The vertical dotted line marks the LSR velocity. The spectral resolution is 1.25 MHz in these figures.

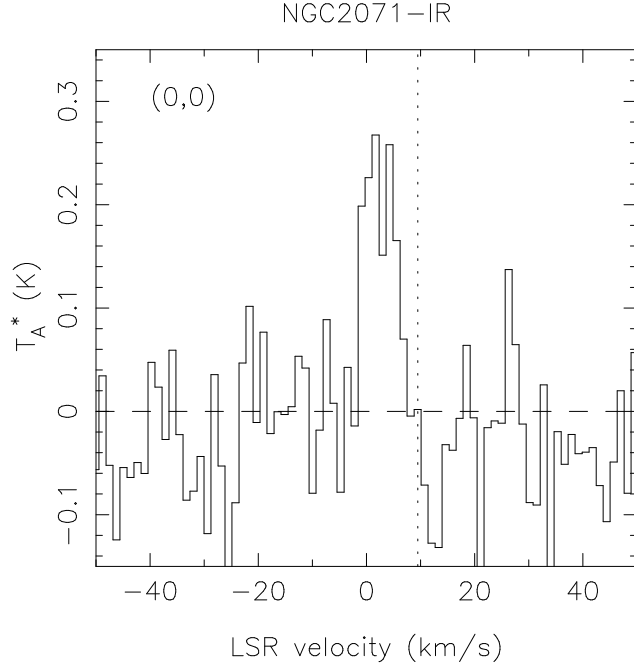


FIG. 7.— SiO 5→4 spectra towards the NGC 2071 outflow. The spectral resolution in this figure is 1.0 MHz. The vertical dotted line marks the LSR velocity.

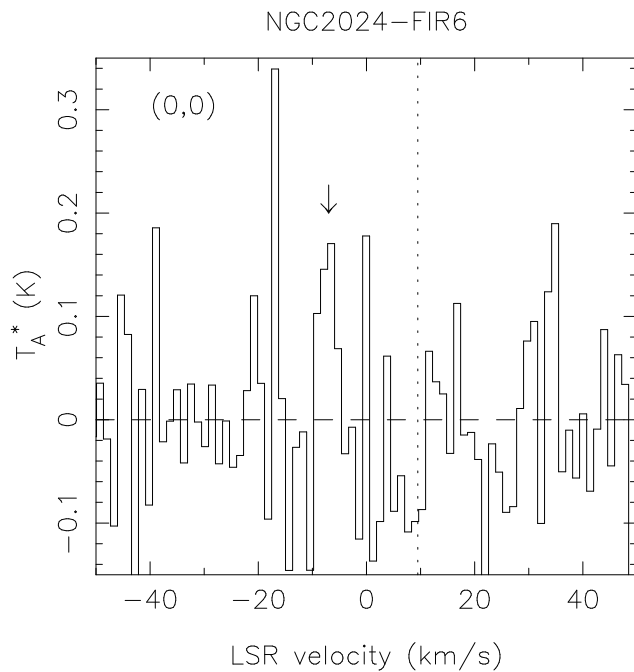


FIG. 8.— SiO 5→4 spectra towards the NGC 2024-FIR6 outflow. The vertical dotted line marks the LSR velocity. The tentative detection is marked by the small arrow at  $-7.2 \text{ km s}^{-1}$ .

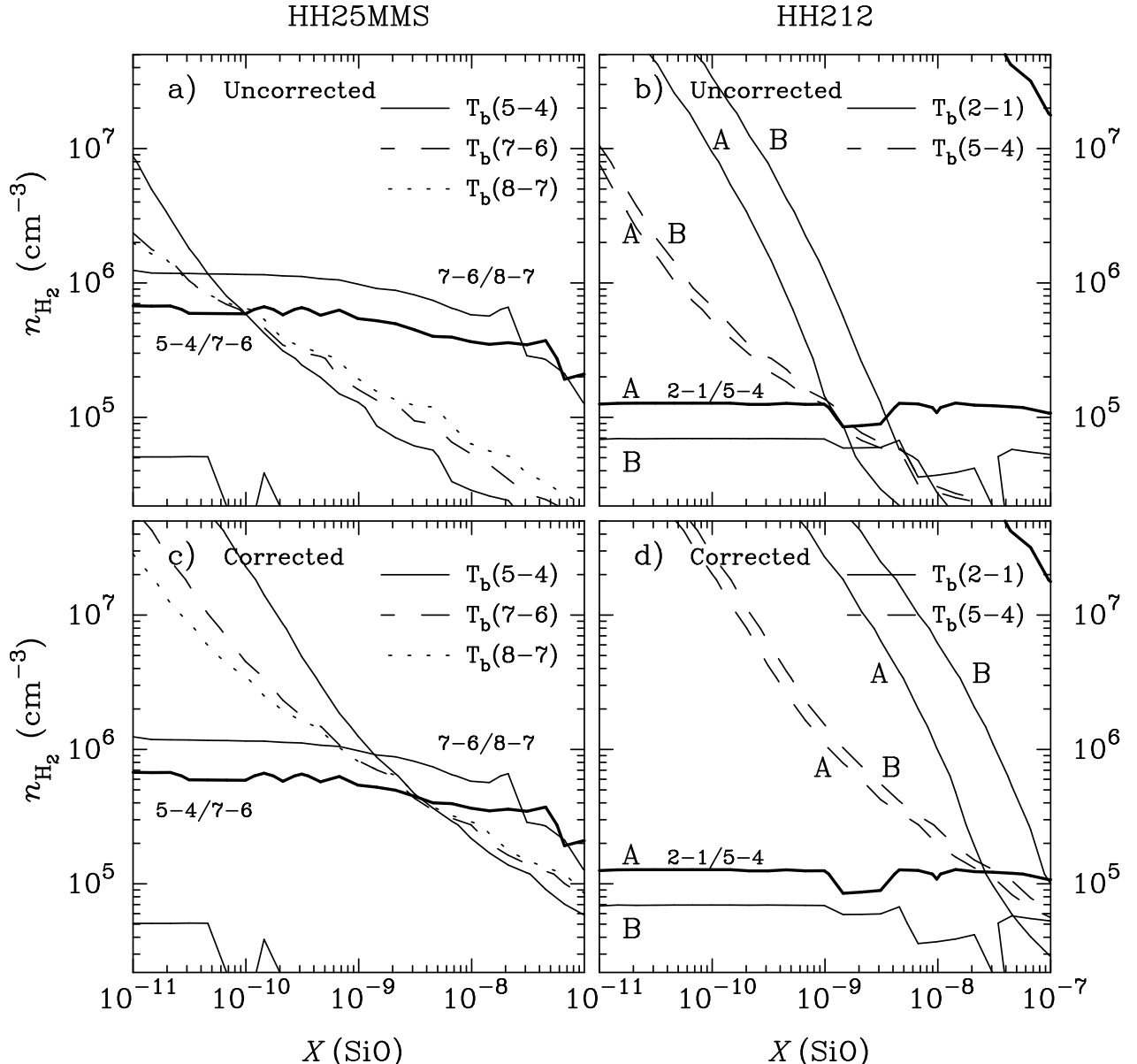


FIG. 9.— Plot of LVG solutions for a kinetic temperature of 100 K for a) and c) HH 25MMS and b) and d) HH 212. In all panels, the contours showing the brightness temperatures run top-left to bottom-right, while the observed line ratios run roughly horizontally across the figure. The top panels show the observed brightness temperatures (Uncorrected), while the lower ones show the brightness temperatures (Corrected) when a beam-dilution correction is applied (multiplied by 20). For the HH 212 figures, the results are given for two positions marked A and B. Position A corresponds to the central position while B corresponds to  $(-8, -18)$ . See text for full details.

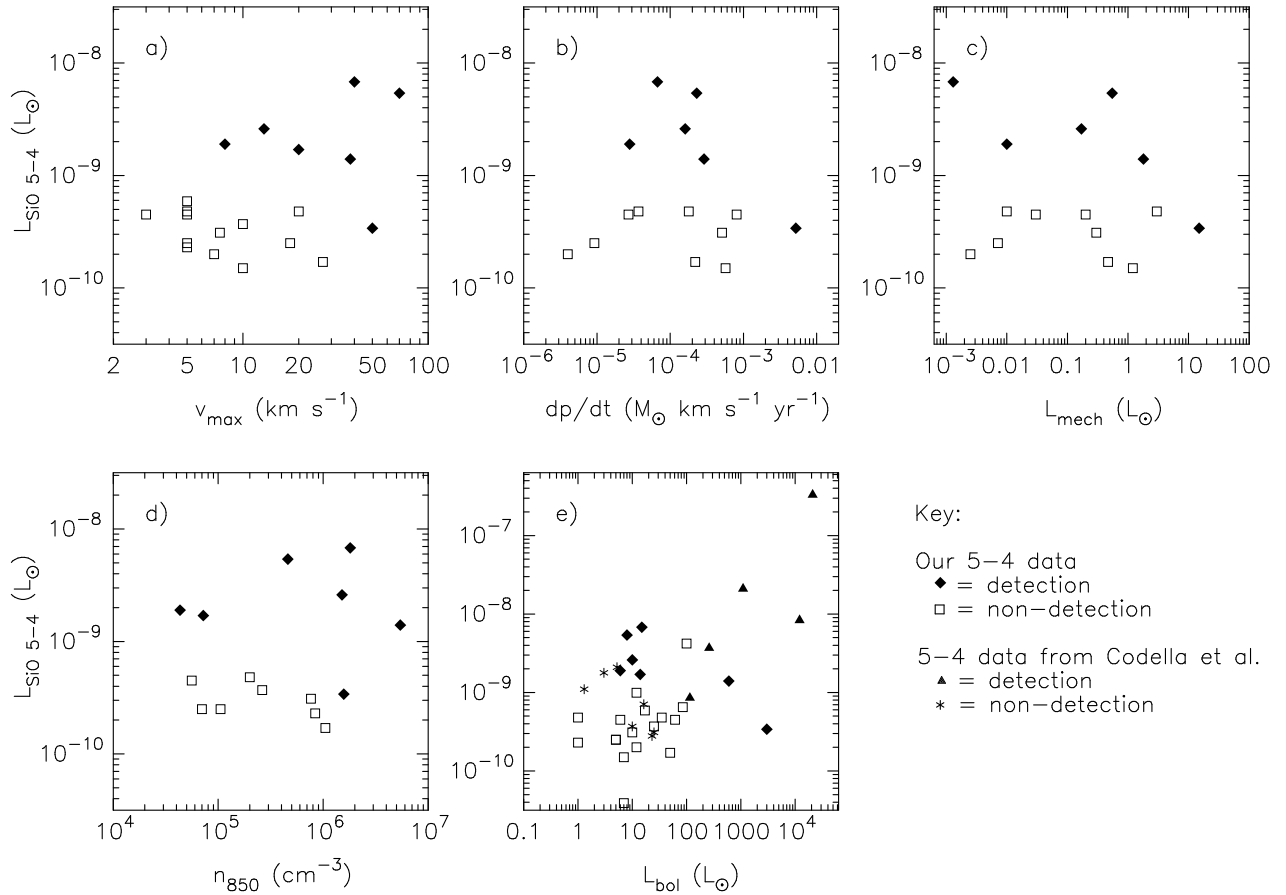


FIG. 10.— Plot of SiO  $J=5\rightarrow 4$  luminosity as a function of source properties a) Maximum velocity, b) outflow force, c) mechanical luminosity and d) submillimetre density. SiO detections are plotted as filled diamonds; upper limits are denoted by open squares. The uncertainties in the outflow parameters are typically a factor of 2–3, somewhat less than the spread in values. The uncertainty in the submillimetre density is a factor of  $\sim 2$ . Panel (e) plots the SiO  $J=5\rightarrow 4$  luminosity as a function of source bolometric luminosity, and includes data from Codella et al. (1999) as triangles.

TABLE 1

SOURCE NAMES, COORDINATES, DISTANCES, LSR VELOCITIES, EVOLUTIONARY CLASS AND PEAK MAIN-BEAM ANTENNA TEMPERATURES AND INTEGRATED INTENSITIES. WHERE NO DETECTION WAS MADE, THE  $1-\sigma$  NOISE LEVEL IS GIVEN FOR A 2.5-MHz WIDE CHANNEL AND THE INTEGRATED INTENSITY IS THIS NOISE OVER A 12-  $\text{km s}^{-1}$  RANGE (EQUAL TO THE MEAN EXTENT OF THE EMISSION IN THE DETECTED SOURCES).

Name	RA(1950)	Dec(1950)	$d$ (pc)	$v_{\text{LSR}}$ ( $\text{km s}^{-1}$ )	Class	Peak $T_{\text{mb}}$ (mK)	$\int T_{\text{mb}} dv$ (K $\text{km s}^{-1}$ )
Detections:							
L1448-mm	03 22 34.3	+30 33 35.0	330	+4.0	0	352	$17.3 \pm 1.4$
HH 211-mm	03 40 48.6	+31 51 24.0	330	+9.0	0	1169	$22.0 \pm 1.1$
V380 Ori-NE	05 34 10.0	-06 40 44.0	450	+8.5	I	436	$4.5 \pm 0.4$
NGC 2024-FIR6	05 39 13.7	-01 57 28.0	415	+10.0	0	330	$0.7 \pm 0.2$
HH 212	05 41 19.0	-01 04 08.0	400	+8.0	0	493	$3.8 \pm 0.6$
HH 25MMS	05 43 33.8	-00 14 36.0	400	+10.0	0	634	$4.2 \pm 0.6$
NGC 2071	05 44 30.7	+00 20 45.0	390	+9.0	I	387	$3.2 \pm 0.6$
Non-detections:							
B5-IRS3	03 43 56.5	+32 33 55.0	350	+10.0	II	<106	<0.68
RNO 15-FIR	03 24 34.9	+30 02 40.0	350	+5.0	0?	<90	<0.58
HH 7-11	03 25 57.9	+31 05 50.0	350	+8.0	I	<79	<0.51
DG Tau	04 24 01.0	+29 59 36.0	140	+6.0	II	<87	<0.56
HL Tau	04 28 44.4	+18 07 35.0	140	+6.5	II	<109	<0.70
L 1634	05 17 21.9	-05 55 05.0	450	+8.0	I?	<159	<1.02
RNO 43-mm	05 29 30.4	+12 47 34.0	450	+9.5	0	<124	<0.79
HH 34-mm	05 33 03.6	-06 28 49.0	450	+8.5	I	<129	<0.83
HH 1-2-mm	05 33 57.0	-06 47 55.0	450	+8.0	I	<126	<0.81
NGC 2024-FIR5	05 39 12.6	-01 57 00.0	415	+10.0	0	<150	<0.96
HH 26IR	05 43 30.5	-00 15 59.0	400	+10.0	I	<85	<0.54
SSV 59	05 43 31.1	-00 15 28.0	400	+10.0	I	<86	<0.55
HH 24MMS	05 43 34.9	-00 11 49.0	400	+10.0	0	<109	<0.70
HH110	05 48 46.8	+02 55 01.0	400	+8.5	I	<53	<0.34
HH111-VLA	05 49 09.3	+02 47 48.0	400	+9.0	I	<126	<0.81
NGC 2264G	06 38 25.8	+09 58 52.0	800	+3.5	0	<86	<0.55
L 1660	07 18 00.9	-23 56 42.0	1500	+20.0	I?	<107	<0.69
Cep E	23 01 10.1	+61 26 16.0	700	-13.0	0	<73	<0.47

Note. — Units of right ascension are hours, minutes and seconds. Units of declination are degrees, minutes of arc and seconds of arc.

TABLE 2

DETAILS OF SOURCE COVERAGE. OFFSETS ARE GIVEN IN ARCSEC FROM THE CENTER POSITION GIVEN IN TABLE 1. REGULAR GRIDS ARE GIVEN IN TERMS OF THEIR EXTENT IN RA AND DEC RESPECTIVELY. STRIP MAPS ARE QUOTED AS THEIR EXTENT ALONG THE FLOW AXIS. LATERAL EXTENT IS ASSUMED TO BE 1 PIXEL UNLESS STATED. POSITIVE EXTENT IS GIVEN ALONG THE DIRECTION OF THE BLUE LOBE. THE POSITION ANGLE (PA) FOR STRIP MAPS IS GIVEN IN DEGREES EAST OF NORTH. NOTE HH25MMS WAS COVERED BY TWO DIFFERENT TYPES OF MAP. POSITIONS IN THE RNO 43-MM FLOW ARE TAKEN FROM BENCE ET AL. (1996).

Name	Map type	PA	Extent
L1448-mm	Point	...	(0,0)
HH 211-mm	Grid	...	-60 to +40, -20 to +30
B5-IRS3	Grid	...	-25 to +25, -25 to +25
RNO 15-FIR	Strip	+42	-100 to +100
HH 7-11	Strip	+119	-100 to +100
DG Tau	Grid	...	-20 to +60, -20 to +0
HL Tau	Grid	...	-20 to +20, -20 to +0
L 1634	Strip	+101	-200 to +200
RNO 43-mm	Grid	...	n1 to s1, n2, n4-n6
HH 34-mm	Strip	+165	+0 to +80
HH 1-2-mm	Grid	...	-80 to +80, -80 to +80
V380 Ori-NE	Strip	+3	-80 to +80
NGC 2024-FIR5	Grid	...	-20 to +40, -80 to +0
NGC 2024-FIR6		...	covered in FIR5 map
HH 212	Strip	+24	-80 to +80
HH 26IR	Strip	+58	-100 to +100
SSV 59		...	covered in HH 25MMS map
HH 25MMS	Strip	+155	-100 to 0
	Grid	...	-20 to 80, -100 to 40
HH 24MMS	Grid	...	-40 to +40, -20 to +0
NGC 2071	Point	...	(0,0)
HH110	Strip	0	-200 to +40
HH111-VLA	Strip	+98	-160 to +200
NGC 2264G	Strip	+94	-100 to +200
L 1660	Strip	+90	-60 to +60
Cep E	Grid	...	-20 to +20, -40 to +40

TABLE 3

ESTIMATED SiO ABUNDANCES TOWARDS THE POSITIONS SPECIFIED OFFSET (IN ARCSEC) FROM THE CENTER POSITIONS GIVEN IN TABLE 1. A CO ABUNDANCE OF  $10^{-4}$  RELATIVE TO H<sub>2</sub> HAS BEEN ASSUMED. CO COLUMN DENSITIES ARE ESTIMATED FROM PUBLISHED DATA.

Source	Position offset	$N_{\text{SiO}}$ (cm <sup>-2</sup> )	$N_{\text{CO}}$ (cm <sup>-2</sup> )	$X_{\text{SiO}}$
L 1448-mm	(0,0)	7.1(12)	8.4(14)	8.5(-7)
HH 211-mm	(-10,5)	2.4(13)	4.6(15)	5.2(-7)
	(15,-5)	1.5(13)	3.7(15)	4.1(-7)
V380 Ori-NE	(0,20)	5.7(12)	2.7(16)	2.1(-8)
	(0,-20)	2.6(12)	2.8(16)	9.3(-9)
HH 212	(0,0)	5.0(12)	5.6(15)	8.9(-8)
	(-8,-18)	4.3(12)	4.0(15)	1.1(-7)
NGC 2024-FIR6	(0,0)	7.1(12)	1.0(16)	7.1(-8)
HH 25MMS	(36,-57)	4.9(12)	4.4(15)	1.1(-7)
	(14,-28)	4.5(12)	1.8(16)	2.5(-8)
NGC 2071	(0,0)	4.5(12)	2.0(16)	2.2(-8)

Note. — The notation  $a(b)$  represents  $a \times 10^b$ .

TABLE 4

SUMMARY OF LVG MODELING. RESULTS ARE PRESENTED FOR EACH POSITION (COLUMN 2) WITHIN EACH SOURCE. THE TRANSITIONS USED, BRIGHTNESS TEMPERATURES AND ASSUMED VELOCITY GRADIENT ARE GIVEN IN COLUMNS 3, 4 AND 5. THE PARAMETER RANGE FOR THE SOLUTIONS IS GIVEN IN COLUMNS 6, 7 AND 8. THESE DATA ARE SHOWN IN FIG. 9A AND B. THE QUANTITY  $X'_{\text{SiO}}$  REPRESENTS THE SiO ABUNDANCE DERIVED FROM THE ‘CORRECTED’ SOLUTIONS (FIG. 9C AND D).

Source	Position offset	Transition	$T_{\text{mb}}$ (K)	$dv/dr$ (km s $^{-1}$ pc $^{-1}$ )	$n_{\text{H}_2}$ (cm $^{-3}$ )	$T_{\text{kin}}$ (K)	$X_{\text{SiO}}$	$X'_{\text{SiO}}$
HH 212-A	(0,0)	2→1	0.23	350	0.8–2.0(5)	50–150	1–3(–9)	2–6(–8)
	(0,0)	5→4	0.26	...	...	...	...	...
HH 212-B	(–8,–18)	2→1	0.60	175	0.7–1.5(5)	50–100	2–5(–9)	5–12(–8)
	(–8,–18)	5→4	0.34	...	...	...	...	...
HH 25MMS	(14,–28)	5→4	0.29	210	0.5–2.0(6)	30–100	2–20(–11)	2–20(–9)
	(14,–28)	7→6	0.12	...	...	...	...	...
	(14,–28)	8→7	0.07	...	...	...	...	...

Note. — The notation  $a(b)$  represents  $a \times 10^b$ .

TABLE 5

DETAILS OF VALUES PLOTTED IN FIG. 10. SiO 5→4 LUMINOSITY (DERIVED FROM THE BRIGHTEST DETECTION GIVEN IN TABLE 1), MAXIMUM OUTFLOW VELOCITY, MOMENTUM FLUX, MECHANICAL LUMINOSITY, SOURCE BOLOMETRIC LUMINOSITY, DYNAMICAL TIMESCALE AND 850- $\mu\text{m}$  LUMINOSITY. IF NO 850  $\mu\text{m}$  MEASUREMENT IS AVAILABLE, ESTIMATES HAVE BEEN MADE FROM OTHER WAVELENGTHS ASSUMING THAT THE FLUX DENSITY IS PROPORTIONAL TO  $\nu^3$  (CHANDLER & RICHER 2000).

Source	$L_{\text{SiO}5\rightarrow4}$ (L $_{\odot}$ )	$v_{\text{max}}$ (km s $^{-1}$ )	$dp/dt$ (M $_{\odot}$ km s $^{-1}$ yr $^{-1}$ )	$L_{\text{mech}}$ (L $_{\odot}$ )	$L_{\text{bol}}$ (L $_{\odot}$ )	$t_{\text{dyn}}$ (yr)	$L_{850\mu\text{m}}$ (L $_{\odot}$ GHz $^{-1}$ )	References
L1448-mm	5.4(–9)	70	2.3(–4)	0.55	8	3.5(3)	1.3(–4)	1,2,3,4,5
HH211-mm	6.8(–9)	40	6.7(–5)	1.3(–3)	15	750	2.1(–4)	3,6
B5-IRS3	<2.3(–10)	5	...	...	...	...	...	5
RNO15-FIR	<2.0(–10)	7	4.0(–6)	2.5(–3)	12	3.1(4)	...	5,7,8
HH7-11	<1.7(–10)	27	2.2(–4)	0.47	50	5.6(3)	2.4(–4)	3,5,9,10
DG-Tau	<3.1(–11)	3.5	1.9(–6)	5.4(–4)	1	3.4(4)	6.1(–7)	5,11
HL-Tau	<3.9(–11)	7	1.7(–5)	9.0(–3)	7	9.0(3)	1.8(–5)	3,5,12,13
L1634	<5.9(–10)	5	...	...	17	...	...	14
RNO43-mm	<4.5(–10)	5	2.7(–5)	0.03	6	3.3(4)	...	5,15
HH34-mm	<4.8(–10)	5	3.7(–5)	0.01	35	1.3(4)	7.9(–5)	16,17,18
HH1-2mm	<4.5(–10)	3	8.1(–4)	0.2	61	1.1(4)	3.6(–5)	5,16,19
V380-Ori-NE	2.6(–9)	13	1.6(–4)	0.17	10	1.6(4)	7.9(–5)	20
NGC2024-FIR5	<4.8(–10)	20	1.8(–4)	3	...	5.0(4)	5.8(–4)	21,22,23
NGC2024-FIR6	3.4(–10)	50	5.2(–3)	15	3(3)	400	3.6(–4)	21,23,24
HH212	1.7(–9)	20	...	...	14	1.4(4)	2.0(–5)	25,26
HH26IR	<2.5(–10)	18	9.2(–6)	7.1(–3)	5	1.3(4)	2.9(–5)	27,28
SSV59	<2.5(–10)	5	...	...	5	...	1.9(–5)	27,28
HH25MMS	1.9(–9)	8	2.8(–5)	0.01	6	1.7(4)	6.7(–5)	28,29
HH24MMS	<3.1(–10)	7.5	5.1(–4)	0.3	10	3.7(4)	1.7(–4)	5,28,30
NGC2071	1.4(–9)	38	2.9(–4)	1.8	600	2.0(4)	1.4(–3)	5,31,32
HH110	<1.5(–10)	10	5.7(–4)	1.2	7	5.0(4)	...	5,33
HH111-VLA	<3.7(–10)	10	...	...	25	...	7.3(–5)	5,34,35
NGC2264G	<9.9(–10)	60	3.2(–4)	1.0	12	4.0(4)	1.2(–4)	5,36,37,38
L1660	<4.2(–9)	4.5	6.6(–4)	0.24	100	2.2(4)	...	5,39
Cep-E	<6.5(–10)	20	3.4(–5)	0.06	85	2.5(4)	9.4(–5)	40

Note. — The notation  $a(b)$  represents  $a \times 10^b$ .

References. — (1) Bachiller et al. 1990; (2) Bachiller et al. 1995; (3) Chandler & Richer 2000; (4) Shirley et al. 2000; (5) Wu, Huang & He 1996; (6) Gueth & Guilloteau 1999; (7) Davis et al. 1997b; (8) Meehan et al. 1998 (9) Knee & Sandell 2000; (10) Bachiller & Cernicharo 1990; (11) Mitchell et al. 1994; (12) Looney et al. 2000; (13) Monin, Pudritz & Lazareff 1996; (14) Davis et al. 1997a; (15) Bence et al. 1996; (16) Chernin & Masson 1995; (17) Stapelfeldt & Scoville 1993; (18) Cohen & Schwartz 1987; (19) Chini et al. 2001; (20) Davis et al. 2000; (21) Chernin 1996; (22) Richer et al. 1989; (23) Visser et al. 1998; (24) Richer 1990; (25) Lee et al. 2000; (26) Zinnecker et al. 1992; (27) Gibb & Heaton 1993; (28) Phillips, Gibb & Little 2001; (29) Gibb & Davis 1998; (30) Chini et al. 1993; (31) Moriarty-Schieven et al. 1989; (32) Mitchell et al. 2001; (33) Reipurth & Olberg 1991; (34) Hatchell et al. 1999; (35) Cernicharo & Reipurth 1996; (36) Lada & Fich 1996; (37) Fich & Lada 1997; (38) Ward-Thompson et al. 1995; (39) Schwartz, Gee & Huang 1988; (40) Ladd & Hodapp 1997.